remote sensing

MDPI

Article

Identifying Major Diurnal Patterns and Drivers of Surface Urban Heat Island Intensities across Local Climate Zones

Yongjuan Guan [1,2], Jinling Quan [1,2,*], Ting Ma [1,2], Shisong Cao [3], Chengdong Xu [1,2] and Jiali Guo [1,2]

[1] State Key Laboratory of Resources and Environmental Information System, Institute of Geographic Sciences and Natural Resources Research, Chinese Academy of Sciences, Beijing 100101, China; guanyongjuan5548@igsnrr.ac.cn (Y.G.); mting@lreis.ac.cn (T.M.); xucd@lreis.ac.cn (C.X.); gjl1521660chd@gmail.com (J.G.)
[2] College of Resources and Environment, University of Chinese Academy of Sciences, Beijing 100190, China
[3] School of Geomatics and Urban Spatial Informatics, Beijing University of Civil Engineering and Architecture, Beijing 100044, China; caoshisong@bucea.edu.cn
* Correspondence: quanjl@lreis.ac.cn

Abstract: Deepening the understanding of diurnal characteristics and driving mechanisms of surface urban heat islands (SUHIs) across different local climate zones (LCZs) and time scales is of great significance for guiding urban surface heat mitigation. However, a comprehensive investigation of SUHIs from the diurnal, local, multi-seasonal, and interactive perspectives remains a large gap. Here, we generalized major diurnal patterns of LCZ-based SUHI intensities (SUHIIs) throughout 2020 over the urban area of Beijing, China, based on diurnal temperature cycle modeling, block-level LCZ mapping, and hierarchical clustering. A geographical detector was then employed to explore the individual and interactive impacts of 10 morphological, socioeconomic, and meteorological factors on the multi-temporal spatial differentiations of SUHIIs. Results indicate six prevalent diurnal SUHII patterns with distinct features among built LCZ types. LCZs 4 and 5 (open high- and mid-rise buildings) predominantly display patterns one, two, and five, characterized by an afternoon increase and persistently higher values during the night. Conversely, LCZs 6, 8, and 9 (open, large, and sparsely built low-rise buildings) mainly exhibit patterns three, four, and six, with a decrease in SUHII during the afternoon and lower intensities at night. The maximum/minimum SUHIIs occur in the afternoon–evening/morning for patterns 1–3 but in the morning/afternoon for patterns 5–6. In all four seasons, the enhanced vegetation index (EVI) and gross domestic product (GDP) have the top two individual effects for daytime spatial differentiations of SUHIIs, while the air temperature (TEM) has the largest explanatory power for nighttime differentiations of SUHIIs. All factor interactions are categorized as two-factor or nonlinear enhancements, where nighttime interactions exhibit notably greater explanatory powers than daytime ones. The strongest interactions are EVI ∩ GDP (q = 0.80) during the day and TEM ∩ EVI (q = 0.86) at night. The findings of this study contribute to an improved interpretation of the diurnal continuous dynamics of local SUHIIs in response to various environmental conditions.

Keywords: surface urban heat island; land surface temperature; local climate zone; geographical detection; diurnal dynamics

Citation: Guan, Y.; Quan, J.; Ma, T.; Cao, S.; Xu, C.; Guo, J. Identifying Major Diurnal Patterns and Drivers of Surface Urban Heat Island Intensities across Local Climate Zones. *Remote Sens.* **2023**, *15*, 5061. https://doi.org/10.3390/rs15205061

Academic Editor: Janet Nichol

Received: 6 July 2023
Revised: 19 October 2023
Accepted: 19 October 2023
Published: 21 October 2023

1. Introduction

Urban heat island (UHI) is a worldwide phenomenon characterized by significantly higher temperatures in cities compared to the surrounding rural areas [1–3]. It has significant impacts on regional climate, energy consumption, air quality, vegetation ecology, and population health [4,5]. Gaining a deeper understanding of the spatiotemporal variations and driving mechanisms of UHIs is crucial for guiding urban thermal management.

Previous studies have mainly relied on a fuzzy urban–rural dichotomy to assess temperature differences [6,7]. However, there is a lack of a consistent standard for urban–

rural division, which has hampered comparisons and led to contradictions among UHI studies [8,9]. Moreover, it is difficult to portray complex intra-urban variability in local thermal environments [10,11]. To describe internal urban structures and properties in a more objective, standardized, and quantitative way [12], Stewart et al. [10] introduced the concept of local climate zones (LCZs), consisting of 17 building types and land cover types with uniform surface covers, structures, materials, and human activities.

LCZ-based UHI studies have been rising in recent years and are divided into two main categories: canopy UHIs (CUHIs) [13–15] and surface UHIs (SUHIs) [8,16,17]. The former mainly reveals the near-surface temperature differences among different LCZ types through station observations [13,18], mobile measurements [14], and numerical simulations [10,15]. However, the spatial representativeness of station observations is usually insufficient, the financial investment in mobile measurements is substantial, and the model uncertainty for realistic scenario simulations can be considerable. Alternatively, others utilized remotely sensed land surface temperature (LST) observations with the advantages of wide coverage and low cost to characterize SUHIs via inter-LCZ comparative analysis [16,19–22]. SUHIs are closely related to, yet distinct from, CUHIs, particularly at the diurnal scale, where they can exhibit contrasting patterns of variation [23,24]. However, due to the limited temporal frequency of fine-resolution LST observations, previous LCZ-based SUHI studies have primarily focused on the annual patterns and several discrete moments [8,17,25], posing challenges in capturing the diurnal continuous dynamics of SUHIs. For instance, Bechtel et al. [8] used LCZs to conduct a comprehensive comparison of SUHIs among 50 global cities at four MODIS overpass times, and Chang et al. [25] examined thermal patterns of each LCZ in Xi'an, China at several moments of ECOSTRESS observations.

Regarding these limitations, researchers have begun to utilize spatiotemporally enhanced LSTs for diurnal investigation. For example, Quan [20] generated hourly 100 m LSTs based on an integrated fusion of Landsat, MODIS, and FengYun-2F LSTs and then analyzed the multi-temporal thermal differences among LCZ types in Beijing, China. However, their analysis focused on LSTs rather than SUHIs. Dong et al. [16], on the other hand, investigated the characteristic parameters of diurnal SUHI intensities (SUHIIs) for built LCZ types in Nanjing, China, via monthly composite diurnal LSTs of 100 m from the combination of spatial downscaling and diurnal temperature modeling. Nevertheless, temporal averaging by month/season/year is somewhat subjective and insufficient to characterize major patterns from complex diurnal dynamics of SUHIIs across varied LCZs and times.

In terms of interpretation of the diurnal SUHII variability, previous studies have often investigated single or multiple drivers through spatial comparative analysis [26] and linear regression/correlation [27,28]. The former compares the SUHI differences among surface categories, which is often used in LCZ-based SUHI studies. However, this method presents challenges in quantifying the contribution of each factor. The latter assumes linear dependencies between SUHI and drivers, whereas there is no strict standard linear correspondence between them, and complex interactions exist during SUHI formation and evolution [29]. Alternatively, the geographical detector (geodetector) measures geographic attributions and driver interactions based on spatial heterogeneity without linear assumptions [30]. The use of geodetector to explore the diurnal SUHII variations would help improve our understanding of the individual and interactive effects of different factors, especially at a diurnal scale; however, such exploration is in great lack [31].

Overall, despite the remarkable progress that has been made, there are still gaps in the generalization of the diurnal continuous variation patterns of SUHIIs across diverse LCZs and the quantification of interactive driving effects behind the spatial differentiations of SUHIIs. Consequently, the current understanding of the variety and taxonomy of the prevalent diurnal SUHII patterns across LCZs remains a large deficiency. To address these issues, here we identify the major diurnal patterns of SUHIIs across different built LCZ types and months in Beijing, China, based on diurnal temperature cycle (DTC) modeling, block-level LCZ mapping, and hierarchical clustering. We then adopt the geodetector to

quantify the individual and interactive impacts of multiple morphological, socioeconomic, and meteorological factors on the spatial stratified heterogeneity of SUHIIs during the day–night and across seasons. The findings of this study contribute to an improved interpretation of SUHI variability in response to the local environment at a diurnal scale and provide valuable insights for enhancing urban thermal regulation.

2. Study Area and Data

2.1. Study Area

Beijing (39°28′N–41°05′N, 115°25′E–117°30′E) covers a total area of 16,410 km^2 with an average altitude of 1000–1500 m in the western and northern mountainous areas and 20–60 m in the southeastern plains. It has a warm, temperate, semi-humid, and semi-arid monsoon climate, experiencing hot and rainy summers and cold and dry winters. The annual average temperature and precipitation in the plain areas are 11–13 °C and 500–600 mm, respectively. Beijing has a dense population of approximately 21.9 million and a high urbanization rate of around 87.5% (Beijing Statistical Yearbook, 2020), and has been exhibiting significant UHI effects for years in the city core area, i.e., around and within the Fifth Ring Road, which was therefore chosen as our main study area (Figure 1).

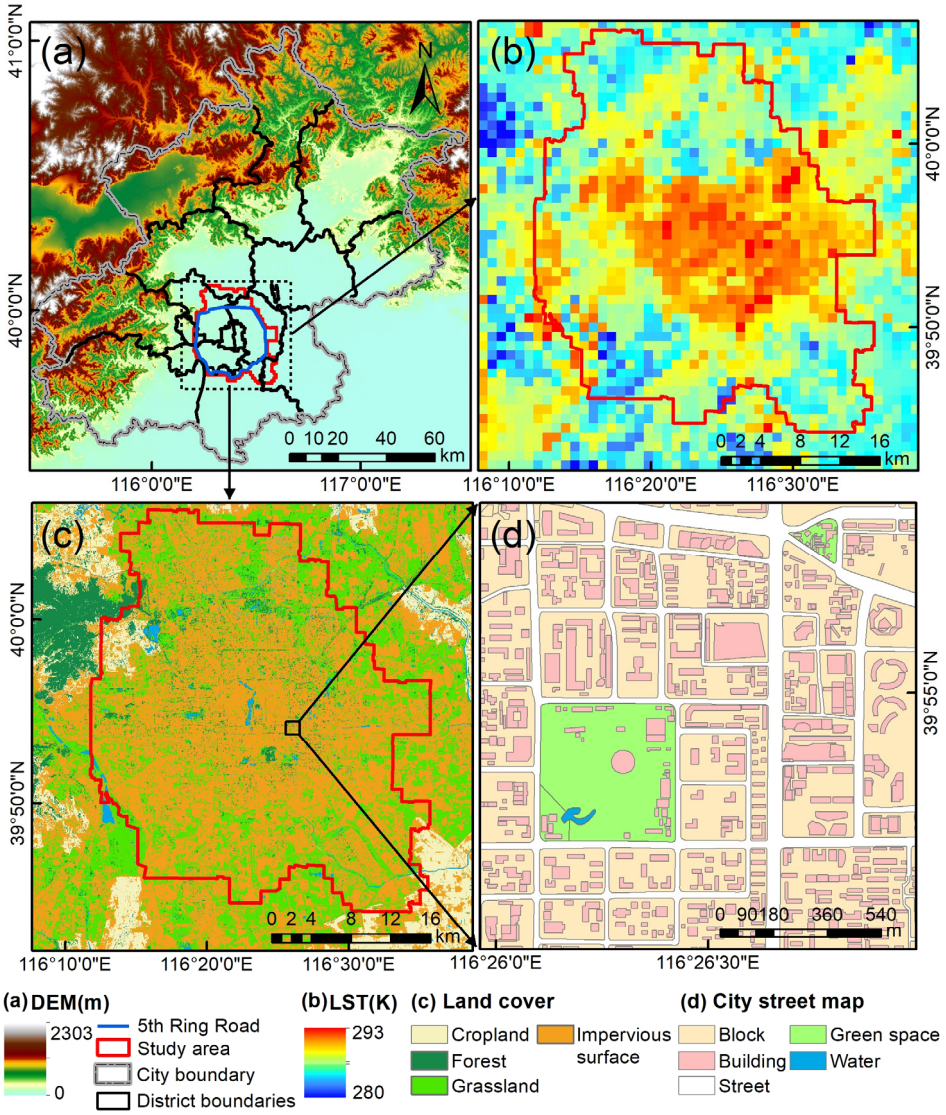

Figure 1. Study area. (**a**) Location and elevations of the study area; (**b**) annual average MODIS land surface temperatures in 2020; (**c**) land cover map (LCM); and (**d**) city street map (CSM).

2.2. Data for DTC Modeling

We downloaded MODIS daily 1 km LST products throughout 2020 (Collection 6.1, https://appeears.eartHD_Batacloud.nasa.gov/, accessed on 16 April 2022), including MOD11A1, acquired at ~10:30 and ~22:30, and MYD11A1, acquired at ~13:30 and ~01:30 local time. These products were retrieved by a generalized split-window algorithm [32] with an overall accuracy within 2 K [33]. Pixels affected by clouds and aerosols were excluded based on the associated QA file. For the DTC modeling over the study area, we selected four consecutive MODIS images with the clearest LST observations per month, i.e., on 30 January, 22 February, 4 March, 30 April, 18 May, 12 June, 23 July, 2 August, 18 September, 18 October, 9 November, and 20 December 2020.

2.3. Data for LCZ Mapping

We obtained a vector-based city street map (CSM, Figure 1d, http://www.navinfo.com/en/aboutus/index.aspx, accessed on 10 March 2022) that contains key attribute information to characterize the urban morphology, including blocks, buildings (height), roads, green spaces, and water. It was converted to 30 m × 30 m grids to match the other two auxiliary data: Landsat 8 and land cover map (LCM). The Landsat 8 data, downloaded from the USGS (http://earthexplorer.usgs.gov/, accessed on 10 March 2022), contain red and near-infrared (VNIR) bands for calculating vegetation fractions. The LCM (Figure 1c) was collected from the Peng Cheng Laboratory (http://data.starcloud.pcl.ac.cn/zh, accessed on 11 March 2022). It was retrieved from the Landsat series through supervised classification, consisting of forest, cropland, grassland, shrubland, water, wetland, impervious land, and bare land. The LCM was mainly used here as a reference for distinguishing vegetation types.

2.4. Driving Factors

A total of 10 morphological [34–36], socioeconomic [27,37], and meteorological [37] factors were selected for the geodetector-based attribution analysis. For the sake of brevity, their details are listed in Table 1, and spatial distributions are shown in Figure 2. The collection of these drivers followed four main criteria: (1) they have demonstrated influences on SUHIs in previous studies; (2) they are easily quantifiable in space and time; (3) they encompass various dimensions and perspectives; and (4) they avoid information redundancy as much as possible. The hourly atmospheric pressure (PRS), relative humidity (RHU), and air temperature (TEM) data were measured at 800 ground stations, interpolated to 1 km grid cell using the spline strategy, and then composed into eight (2 × 4) datasets to facilitate daytime (08:00–16:00) and nighttime (20:00–04:00) analysis across four seasons. The monthly enhanced vegetation index (EVI) data were also aggregated to a seasonal scale but served as a common independent variable for both day and night. The yearly data, including modified normalized difference water index (MNDWI), building surface fraction (BSF), mean building height (BH), gross domestic product (GDP), population density (PD), and road density (RD), were used as constants throughout days and seasons.

Table 1. Details on the driving factors.

Indicator	Description	Temporal Resolution	Spatial Resolution	Source	Calculation
Morphological Factors					
EVI	Enhanced vegetation index	Monthly	500→1000 m	MOD13A3 [1]	
MNDWI [2]	Modified normalized difference water index	Yearly	10→1000 m	Sentinel 2	(Green–MIR)/(Green+MIR)
BSF	Building surface fraction	Yearly	10→1000 m	CSM	Total building area/grid area [3]
BH	Mean building height	Yearly	10→1000 m	CSM	Total building height/total building numbers

Table 1. *Cont.*

Indicator	Description	Temporal Resolution	Spatial Resolution	Source	Calculation
Socioeconomic Factors					
GDP	Gross domestic product	Yearly	1000 m	RESDC [4]	
PD	Population density	Yearly	1000 m	RESDC	
RD	Road density	Yearly	1000 m	CSM	Total road area/grid area
Meteorological Factors					
PRS	Atmospheric pressure	Hourly	Site→1000 m	CMDC [5]	Spline interpolation
RHU	Relative humidity	Hourly	Site→1000 m	CMDC	Spline interpolation
TEM	Air temperature	Hourly	Site→1000 m	CMDC	Spline interpolation

[1] downloaded from https://appeears.earthdatacloud.nasa.gov/, accessed on 4 June 2022. [2] calculated from all clear-sky Sentinel 2 data in 2020 and averaged to a yearly dataset. [3] grid area = 1 km × 1 km. [4] Resource and Environment Science and Data Center (http://www.resdc.cn, accessed on 19 September 2022). [5] China Meteorological Data Service Center (https://data.cma.cn/en, accessed on 10 October 2022).

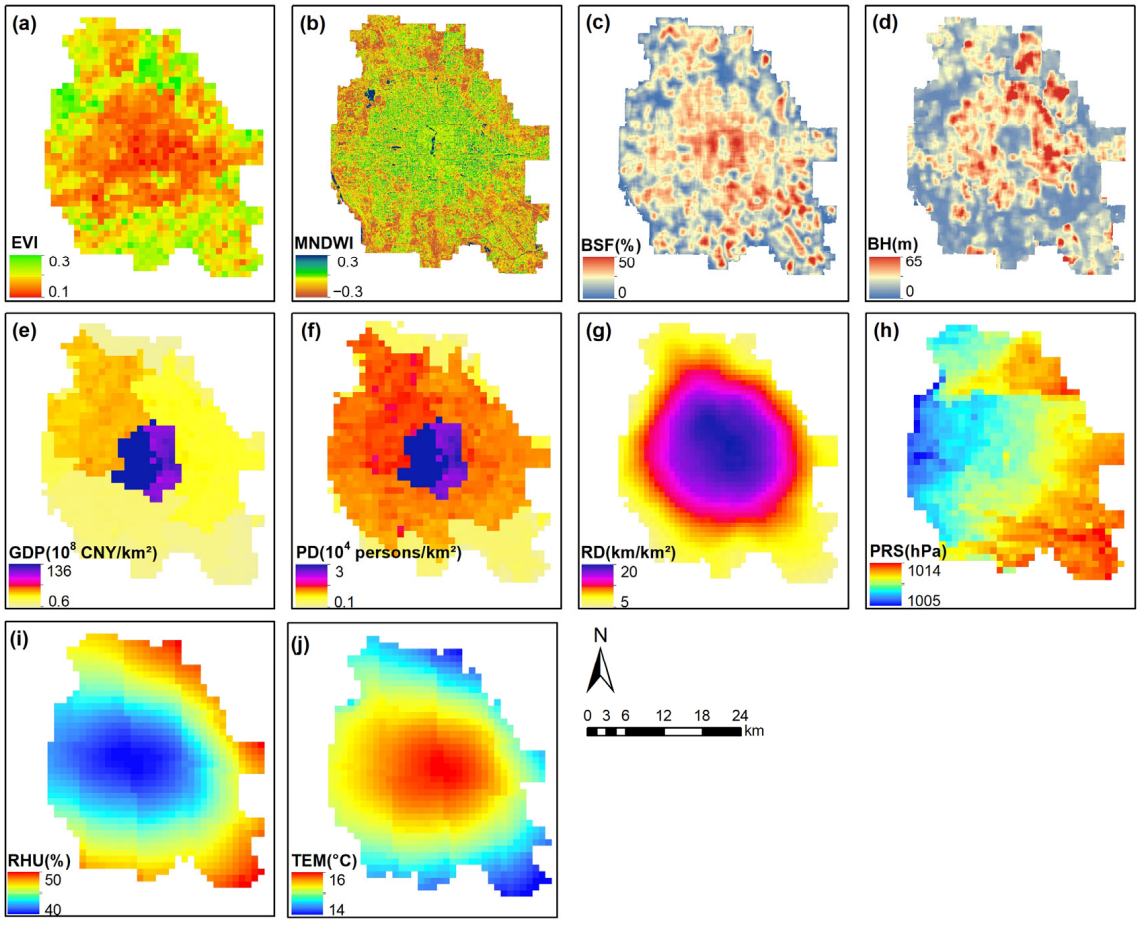

Figure 2. Spatial distributions of the driving factors at a yearly scale. (**a**) Enhanced vegetation index (EVI); (**b**) Modified normalized difference water index (MNDWI); (**c**) Building surface fraction (BSF); (**d**) Mean building height (BH); (**e**) Gross domestic product (GDP); (**f**) Population density (PD); (**g**) Road density (RD); (**h**) Atmospheric pressure (PRS); (**i**) Relative humidity (RHU); and (**j**) Air temperature (TEM).

3. Methodology

The research framework of this study consists of four main steps (Figure 3): (1) reconstruction of diurnal LSTs based on the selected MODIS LSTs and a modified four-parameter DTC model; (2) classification of LCZs by a GIS-based block-level mapping

approach [38] for built-up and land-cover types; (3) identification of major diurnal patterns of SUHIIs across different LCZs and months; and (4) geographical detection of SUHII differentiations with 10 driving factors at multiple time scales.

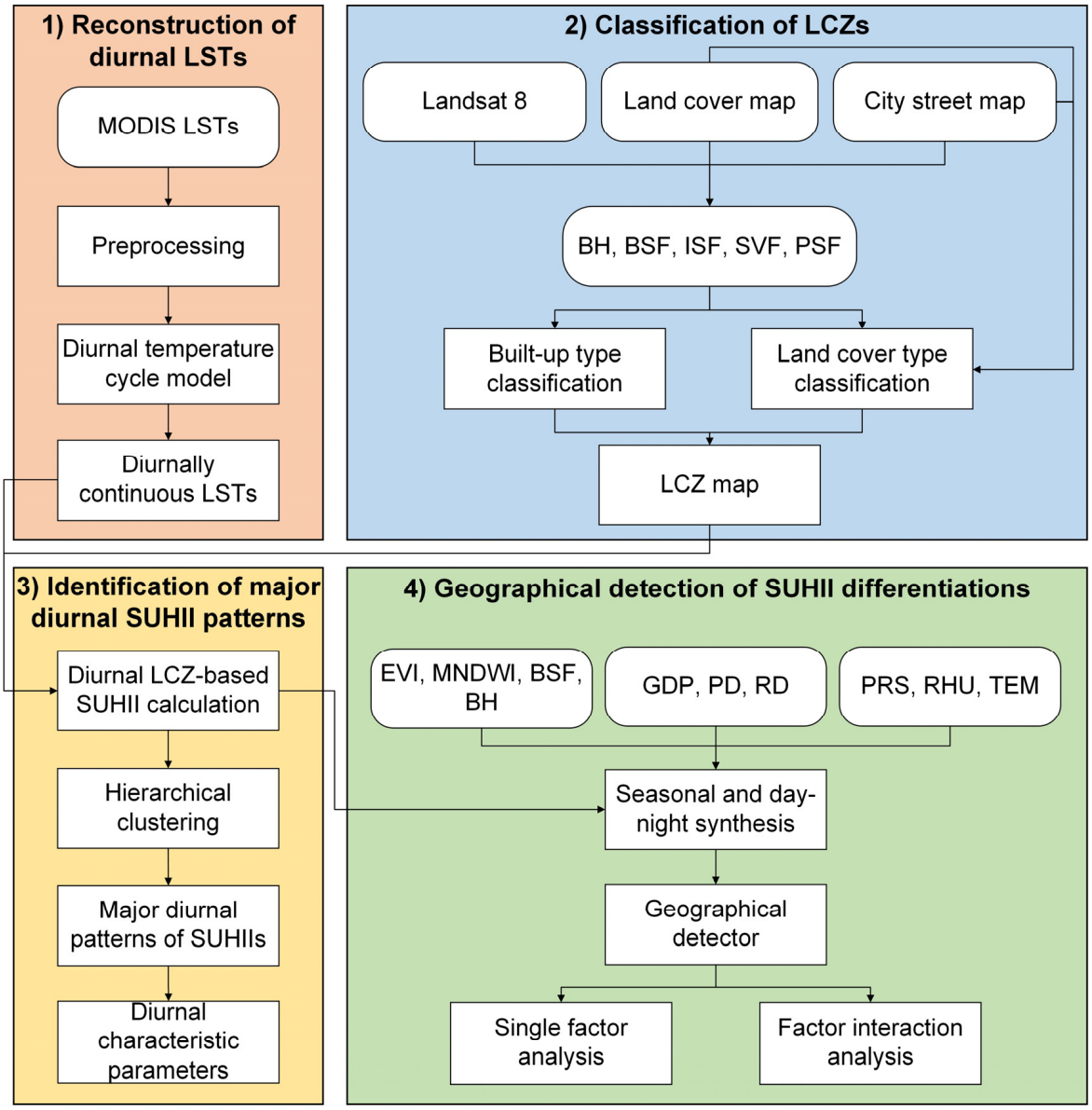

Figure 3. Flowchart of this study.

3.1. Reconstruction of Diurnal LSTs

Many DTC models have been proposed to reconstruct diurnal continuous LSTs from sporadic thermal observations with four or more parameters [39–44]. There is usually a trade-off between applicability and accuracy [45,46]. Given the maximum of four MODIS observations per day and the focus of this study on major patterns across seasons, the model proposed by Inamdar et al. [43] was adopted with a zero assumption on the temperature difference between adjacent sunrise times [39]. Specifically, the diurnal temperature variation with time ($T(t)$) is described as a combination of harmonic and hyperbolic functions based on thermal diffusion and Newton's cooling law:

$$T(t) = \begin{cases} T_{\text{day}}(t) = T_0 + T_{\text{a}} \cos\left[\left(\frac{\pi}{\omega}\right)(t - t_m)\right], t < t_s \\ T_{night}(t) = T_0 + \left[T_{\text{a}} \cos\left(\frac{\pi}{\omega}(t_s - t_m)\right)\right] \frac{k}{(k+t-t_s)}, t \geq t_s \end{cases} \quad (1)$$

with

$$\begin{cases} \mathrm{k} = \frac{\omega}{\pi}\tan^{-1}\left(\frac{\pi}{\omega}(t_s - t_m)\right) \\ \omega = \frac{2}{15}\arccos(-\tan\phi\tan\delta) \\ \delta = 23.45\sin\left(\frac{360}{365}(284 + DOY)\right) \end{cases}$$

where T_0 is the lowest early morning temperature; T_a is the diurnal temperature amplitude; t_m is the time when the temperature reaches its maximum; t_s is the time when the temperature begins to decay freely; ω represents the half period of the cosine term; k is the attenuation constant; ϕ is the latitude; δ is the solar declination; and DOY is the day of year.

T_0, T_a, t_m and t_s are the four unknown parameters, which were solved pixel-by-pixel with the nonlinear least square fitting method in MATLAB using the four MODIS LST images selected per month (Section 2.2). Subsequently, diurnally continuous LSTs were reconstructed for the specified day each month by substituting the solved parameters into Equation (1).

3.2. Classification of LCZs

The study area was classified into 15 LCZ types using a simple GIS-based block-level mapping method we proposed previously [38]. The basic idea of this approach is to calculate five key morphological and coverage indicators for each block, based on which blocks are hierarchically assigned with the most appropriate LCZ types regarding their typical ranges defined in the LCZ scheme. The five indicators include BSF, BH, pervious surface fraction (PSF), impervious surface fraction (ISF), and sky view factor (SVF). They were calculated from the CSM attributes, Landsat VNIR bands, and LCM and averaged for each block. The hierarchical classification principle is illustrated in Figure 4: LCZs 1, 2, 4, 5, and 9 were first distinguished based on BSF and BH; LCZs 3, 6, 7, and 8 were then classified by combining BSF, BH, and one of the remaining indicators; and finally blocks with BH < 10 m and BSF < 10% were classified as LCZs A–G according to the natural land surface types provided in CSM and LCM. More details on the approach can be found in Quan [38].

3.3. Identification of Major Diurnal Patterns of SUHIIs

As one of the most representative indicators for SUHI, the SUHII was calculated hour-by-hour for different LCZs based on the diurnal LST data and LCZ map generated earlier. Specifically, the LCZ-based SUHII is defined as the average LST difference between a specific built LCZ type and a land cover type (typically LCZ D) [16,19]:

$$SUHII(t)_{LCZX} = \frac{\sum_{i=1}^{m} T(i,t)_{LCZX}}{m} - \frac{\sum_{j=1}^{n} T(j,t)_{LCZD}}{n} \quad (2)$$

where $SUHII(t)_{LCZX}$ represents the SUHII of LCZ X at time t; $T(i,t)_{LCZX}$ and $T(j,t)_{LCZD}$ denote the LSTs of pixel i in LCZ X and pixel j in LCZ D at t, respectively; m and n are the total numbers of i and j, respectively. Herein, X = 4, 5, 6, 8, and 9, while other built LCZ types were excluded from this calculation owing to their insufficient samples in the study area in comparison to those of LCZ D.

To identify the major diurnal patterns of SUHIIs across different LCZs and months, a hierarchical clustering analysis was performed on the 60 groups (12 months × 5 main built LCZ types) of diurnal SUHII curves. Specifically, each of the samples was initially assigned to a separate class, and those with the smallest distance were merged iteratively to form a comprehensive class. There are several methods to measure the distance between classes. In this study, the longest distance was adopted according to the practical clustering performance, and the sum of distances and a similarity of 40 were employed as the criteria for clustering centroids and divisions. Five characteristic parameters were then calculated for each clustered diurnal pattern, including the maximum SUHII ($I_{\max}$), minimum SUHII ($I_{\min}$), nocturnal (20:00–04:00) average SUHII (I_{night}), time of $I_{\max}$ ($t_{\max}$), and time of $I_{\min}$ ($t_{\min}$).

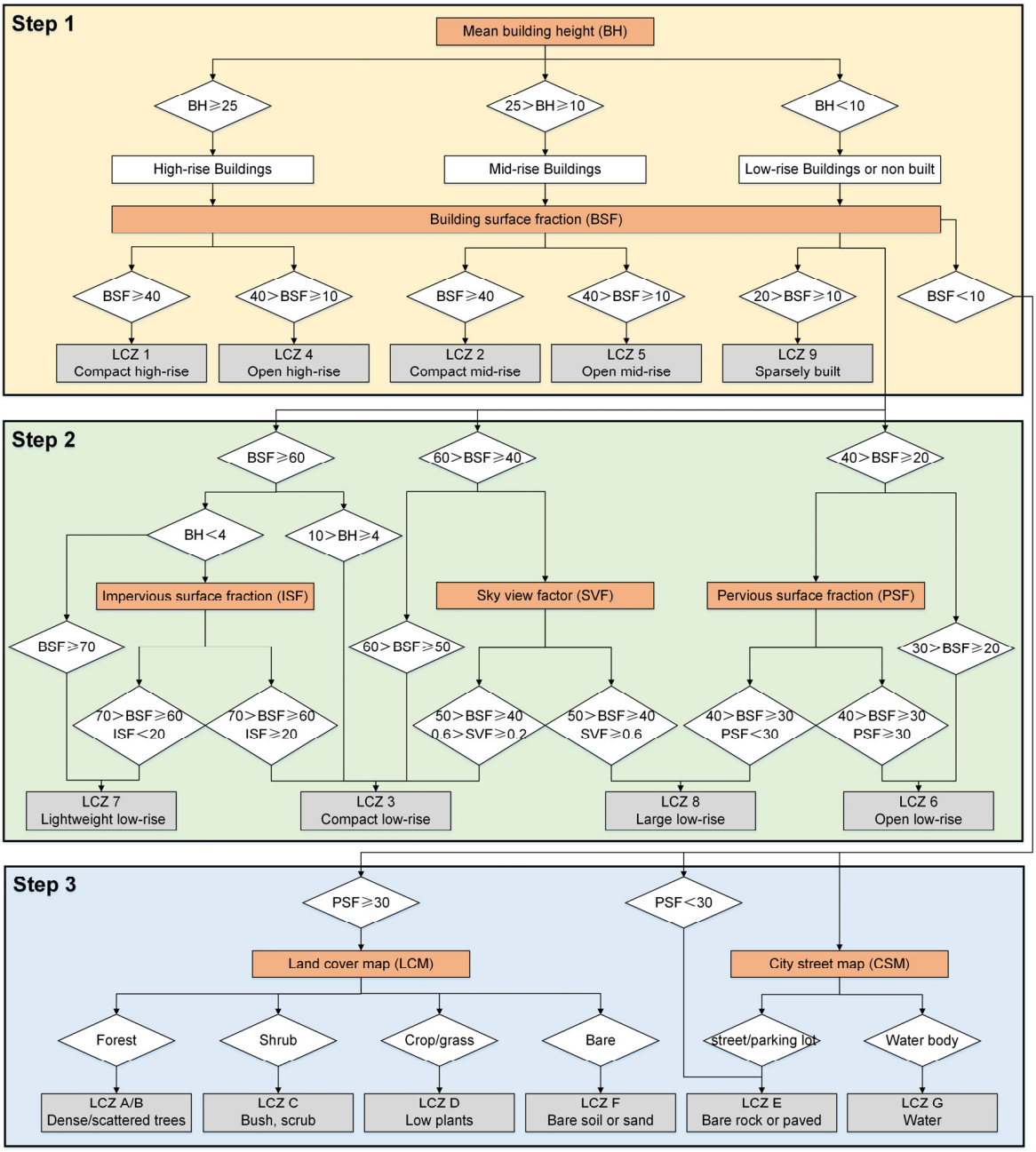

Figure 4. Hierarchical classification of LCZs according to the five indicators, CSM and LCM.

3.4. Geographical Detection of SUHII Differentiations

The geodetector *q* statistic was applied to analyze the spatial stratified heterogeneity of SUHIIs and their driving mechanisms across different seasons and day–night periods [47]. The basic concept is that if independent variables significantly affect the dependent variable, they would have consistent spatial distribution characteristics and stratified heterogeneity [48]. The *q* statistic can be expressed as follows:

$$q(X) = 1 - \frac{\sum_{h=1}^{L} N_h \sigma_h^2}{N\sigma^2} \quad (3)$$

where h is the layer Y based on X stratification; L is the total number of layers; N and N_h are the numbers of pixels in the entire region and layer h, respectively; σ^2 and σ_h^2 are the variances of Y in the entire region and layer h, respectively. The calculation software and

tutorial can be found on the Geodetector Learning website at http://www.geodetector.cn/, accessed on 30 September 2023.

Herein, the Y variable represents the seasonal daytime (08:00–16:00) and nighttime (20:00–04:00) average SUHIIs at the pixel level, with respect to the average LST in LCZ D. The X variable is one of the 10 driving factors (Table 1). Each X was stratified into 9 layers using a quantile classification method. The resultant q ranges from 0 to 1, indicating the individual explanatory power of a given factor X on the spatial stratified heterogeneity of SUHIIs, expressed as $q \times 100\%$. By further calculating and comparing $q(X_1)$, $q(X_2)$, and $q(X_1 \cap X_2)$, the interaction effect of any two factors can be determined, as shown in Table 2.

Table 2. Types of interactions between two variables.

Creterion	Interaction Type
$q(X_1 \cap X_2) < \text{Min}(q(X_1), q(X_2))$	Nonlinear weakening
$\text{Min}(q(X_1), q(X_2)) < q(X_1 \cap X_2) < \text{Max}(q(X_1), q(X_2))$	Single-factor nonlinear weakening
$q(X_1 \cap X_2) > \text{Max}(q(X_1), q(X_2))$	Two-factor enhancement
$q(X_1 \cap X_2) = q(X_1) + q(X_2)$	Independent
$q(X_1 \cap X_2) > q(X_1) + q(X_2)$	Nonlinear enhancement

4. Results

4.1. A general View of the LCZs and Corresponding LSTs

The four DTC parameters (T_0, T_a, t_m and t_s) derived for the 12 months are illustrated in Figure 5. T_0 reaches its peak in summer (close to 300 K) and slump in winter (<275 K). The overall trend accords with the annual temperature cycle driven by solar radiation in Beijing. T_a mostly ranges from 15 K to 20 K, while dropping by 1–3 K in August, December, and January, i.e., the hottest and coldest months. t_m (11:00–14:00) and t_s (15:00–18:00) have similar monthly variations, indicating that an earlier temperature peak is usually accompanied by an earlier temperature decay and vice versa. The absolute fitting error in comparison to the MODIS input is 0.76 K. The resulting hourly LSTs were further compared to the hourly seamless LST product (0.02°) generated by Cheng et al. [49], yielding a mean absolute difference of 2.52 K.

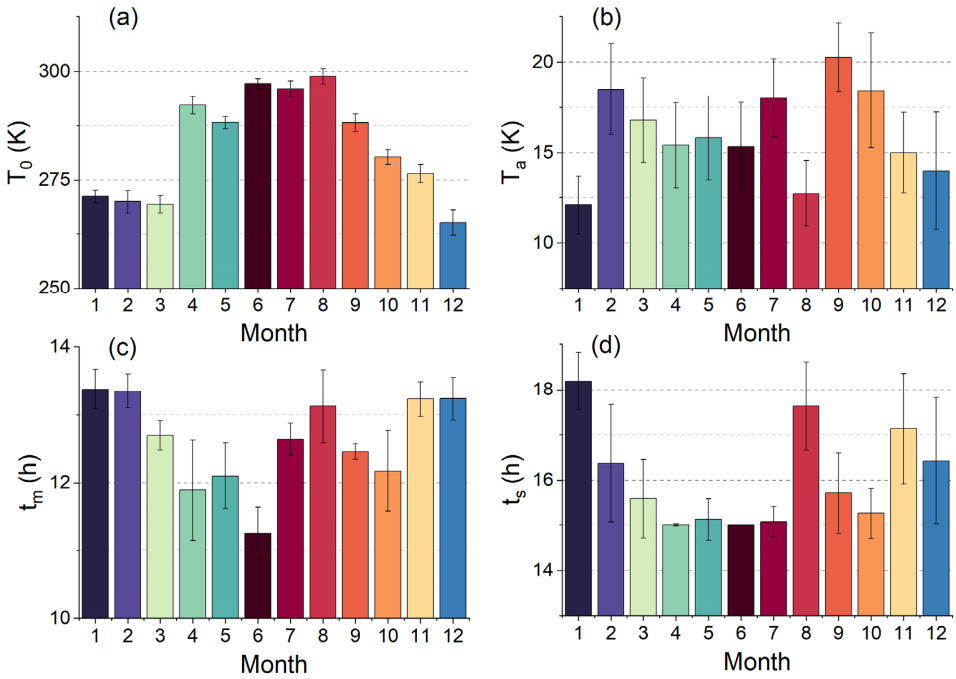

Figure 5. Monthly Distribution of T_0, T_a, t_m, and t_s. (**a**) T_0 is the lowest early morning temperature; (**b**) T_a is the diurnal temperature amplitude; (**c**) t_m is the local time when the temperature reaches its maximum; and (**d**) t_s is the local time when the temperature begins to decay freely.

Figure 6 shows the LCZ map generated over the study area. Previous validation against field samples reveals an agreement of ~90% [38]. The dominant built LCZ types are open high-rise (LCZ 4), open mid-rise (LCZ 5), open low-rise (LCZ 6), large low-rise (LCZ 8), and sparsely built (LCZ 9), each accounting for more than 5% of the total. Among them, LCZ 5 is the most widely distributed (28.8%), followed by LCZ 6 (12.9%). These five built LCZ types were selected for subsequent LCZ-based SUHII calculations considering the sufficient samples that are comparable to those of LCZ D (low plants, 4.7%). In terms of spatial distributions, Figure 6 shows a general progression from low-rise to mid-rise and then to low-rise again, moving from the center to the outskirts. Specifically, the central area consists mainly of open low-rise buildings (LCZ 6), encompassing landmarks like the Forbidden City and Hutongs. Extending towards the Third and Fourth Ring Roads, open mid-rise buildings (LCZ 5) become more prevalent, interspersed with open high-rise buildings (LCZ 4). Continuing towards the Fifth Ring Road, a mixed distribution of open low-rise buildings (LCZ 6) and sparse buildings (LCZ 9) is observed. Vegetation types (LCZs A–D) mainly comprise parks and farmlands scattered in the surroundings.

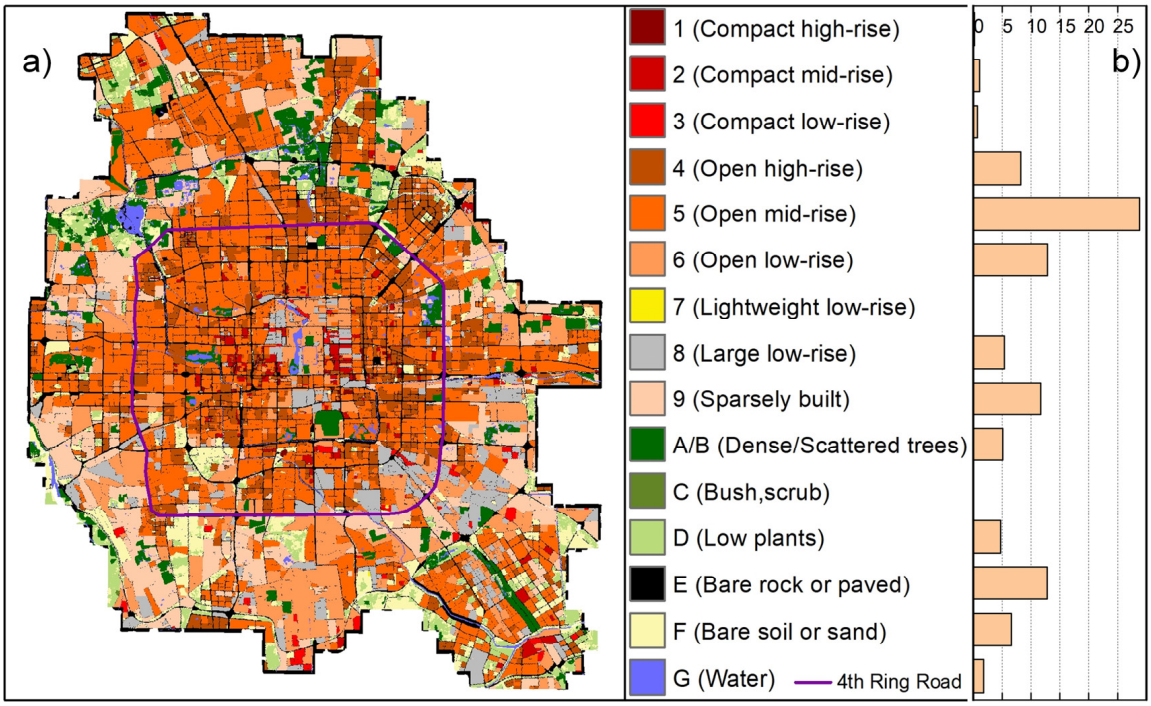

Figure 6. Local climate zones (LCZs) of the study area. (**a**) shows the LCZ map and (**b**) lists the proportion (%) of each LCZ type.

Combining the LCZ map and diurnal LSTs, Figure 7 exhibits distinct thermal characteristics of various LCZs during the day and night. The LST differences among LCZs are relatively small and generally stable during the daytime (except for spring), while the nighttime shows significant variability. At night, the LSTs of both compact (LCZs 1–3) and open buildings (LCZs 4–6) decline with decreasing building height, with compact buildings being more affected in summer and winter. During the daytime, the thermal impact of building height on compact buildings is generally negative in spring and summer and less significant in autumn and winter. This is consistent with previous findings that growing building height decreases daytime LSTs and increases nighttime LSTs [25,34]. Furthermore, for high-rise buildings, compact ones tend to have higher LSTs than open ones. From an average perspective, vegetation types (LCZs A/B and D) generally have lower LSTs than built LCZ types for all seasons and day–night periods (except for spring), suggesting that a SUHI phenomenon constantly controls the study area.

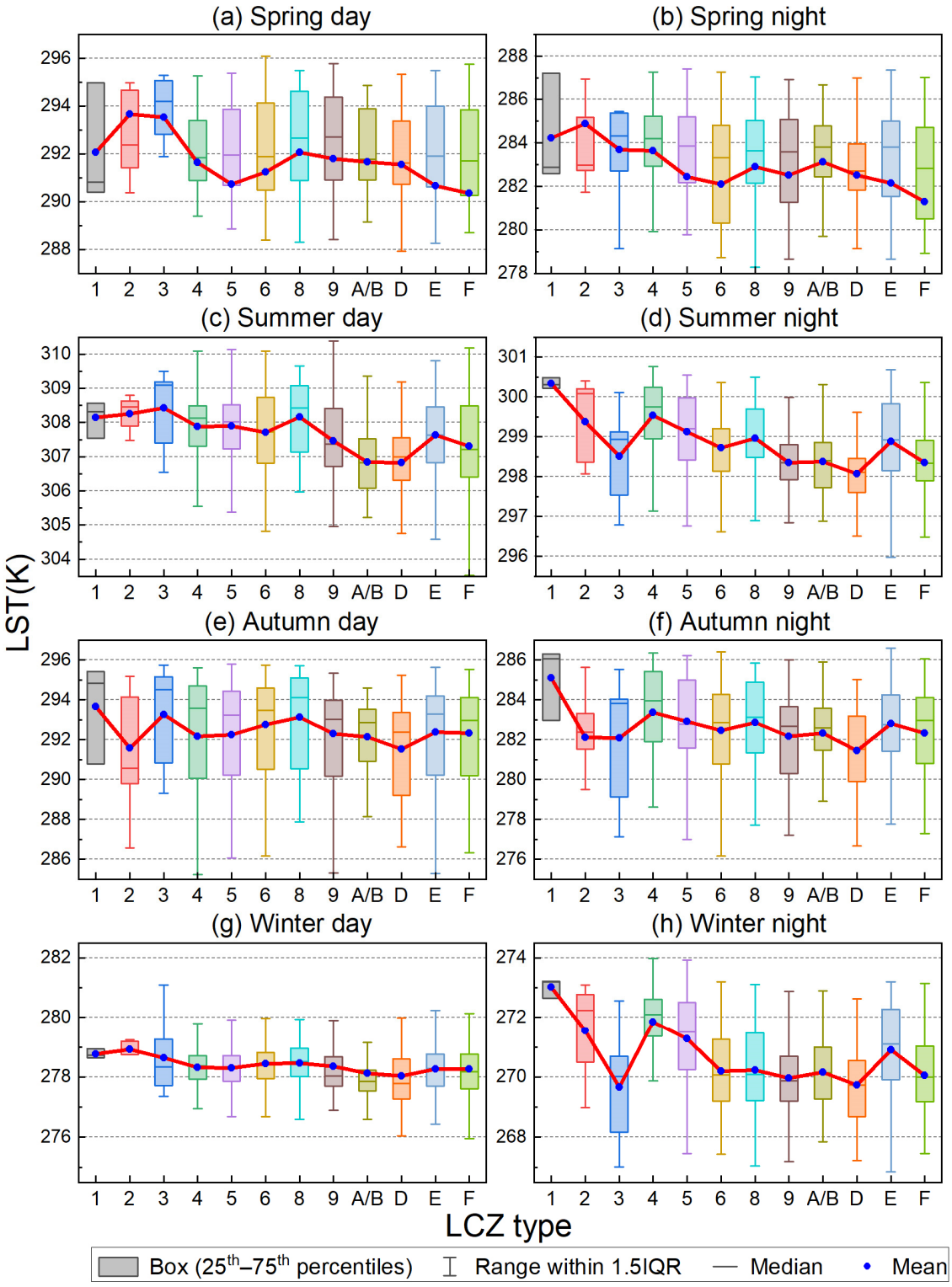

Figure 7. Thermal characteristics of different LCZs during the daytime (08:00–16:00) and nighttime (20:00–04:00) in four seasons.

4.2. Diurnal Patterns of SUHIIs across Different LCZs and Months

Figure 8 shows the diurnal variations of SUHIIs of five main built LCZ types (LCZs 4, 5, 6, 8, and 9) in 12 months and four seasons. It illustrates a similar diurnal pattern between LCZs 4 (open high-rise) and 5 (open mid-rise), which is characterized by a rapid decrease in the morning, followed by a sharp increase in the afternoon, peaking around 18:00, and

then exhibiting slow changes during the night. However, there are differences between the seasons. Specifically, for LCZs 4 and 5, the diurnal SUHII amplitudes in autumn and winter are larger than those in spring and summer, and an overall increasing/decreasing trend in SUHII after ~18:00 is presented in summer/autumn. As for SUHIIs of LCZs 6 (open low-rise), 8 (large low-rise), and 9 (sparsely built), the variations after ~15:00 are consistent throughout the seasons, i.e., SUHIIs decrease from ~15:00 to ~19:00 and remain low at night; however, the patterns from ~9:00 to ~15:00 are rather different, with a predominant decrease in spring and summer but an increase in autumn and winter. Meanwhile, the diurnal variations of LCZ-based SUHIIs significantly differ within seasons [16]. Specifically, in March and April, the SUHII variation in each LCZ accords closely with its average in spring; however, in May, the patterns are opposite to its seasonal average. For the months of June–August, the diurnal SUHII patterns are similar to the summer average, but LCZs 6, 8, and 9 exhibit peak values around 15:00 in August, while the peak values occur between 8:00 and 12:00 in June and July. In autumn, there are substantial differences in SUHIIs among various built LCZ types across months, but both LCZs 4 and 5 show sharp peaks around 18:00 throughout the season. The winter months experience the most stable and consistent diurnal SUHII patterns for a given LCZ type. Notably, LCZ 4 exhibits a cold island phenomenon between 10:00 and 14:00 in December and January, which may be partially attributed to shading effects from high-rise buildings [50,51].

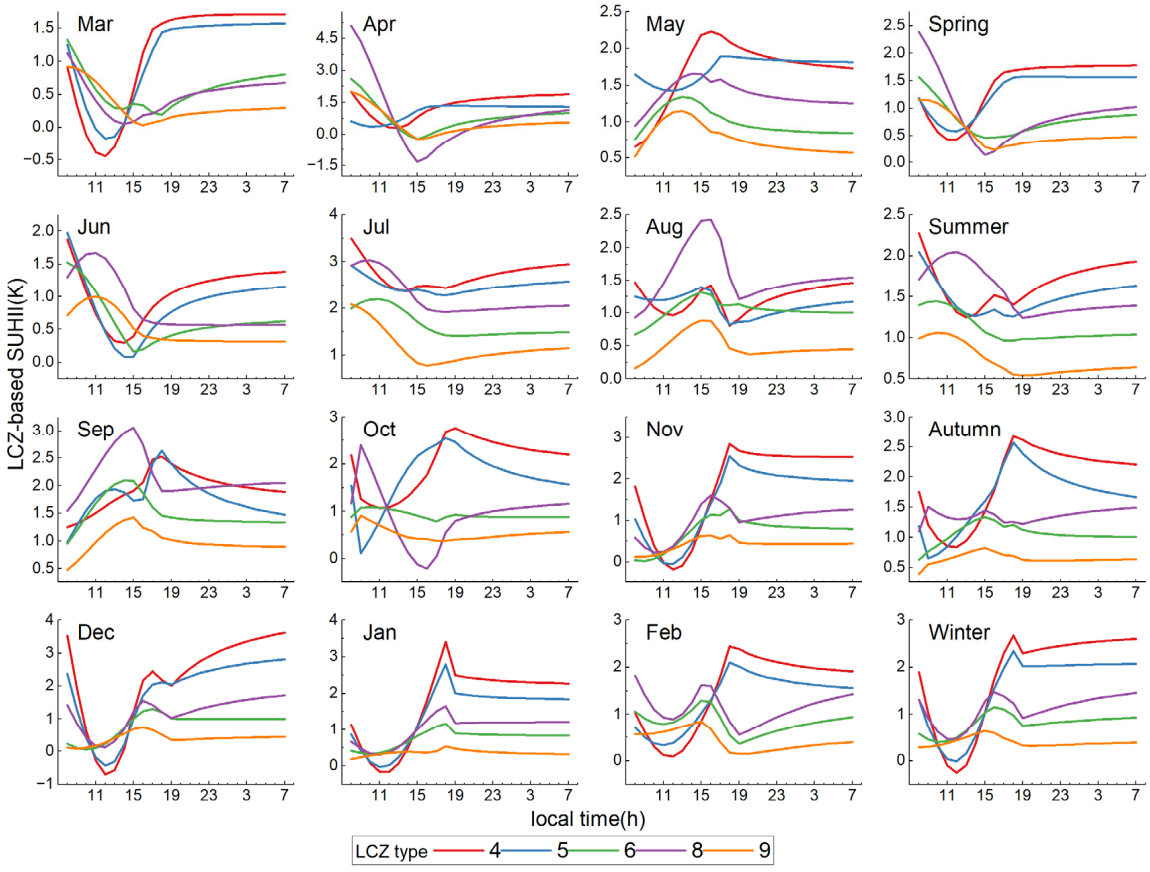

Figure 8. Diurnal SUHIIs of five main built LCZ types (LCZs 4, 5, 6, 8, and 9) in 12 months and four seasons.

It can be seen that the seasonally averaged diurnal curve, a common approach in previous studies, still has some insufficiency and complexity in expressing major diurnal patterns of SUHIIs across different LCZs and months. In order to promote a more general understanding of these variation characteristics, a hierarchical clustering analysis was conducted (Section 3.3), and six primary diurnal patterns with distinct features were identified (Figures 9–11). In general, LCZs 4 and 5 predominantly display patterns one,

two, and five, characterized by an afternoon increase in SUHII, which then sustains at higher values at night (I_{night} > 1.2 K). Conversely, LCZs 6, 8, and 9 mainly exhibit patterns three, four, and six, showing a decrease in SUHII during the afternoon hours and lower intensities at night ($I_{night} \leq$ 1.2 K), except that during November–January, pattern two dominates instead probably due to increased LSTs in these low-rise buildings caused by extensive winter heating. Moreover, opposite trends in the timing of extreme SUHIIs are observed between patterns 1–3 and patterns 5–6: t_{max} and t_{min} for patterns 1–3 occur in the afternoon/evening and morning, respectively, whereas for patterns 5–6, they appear in the morning and afternoon, respectively.

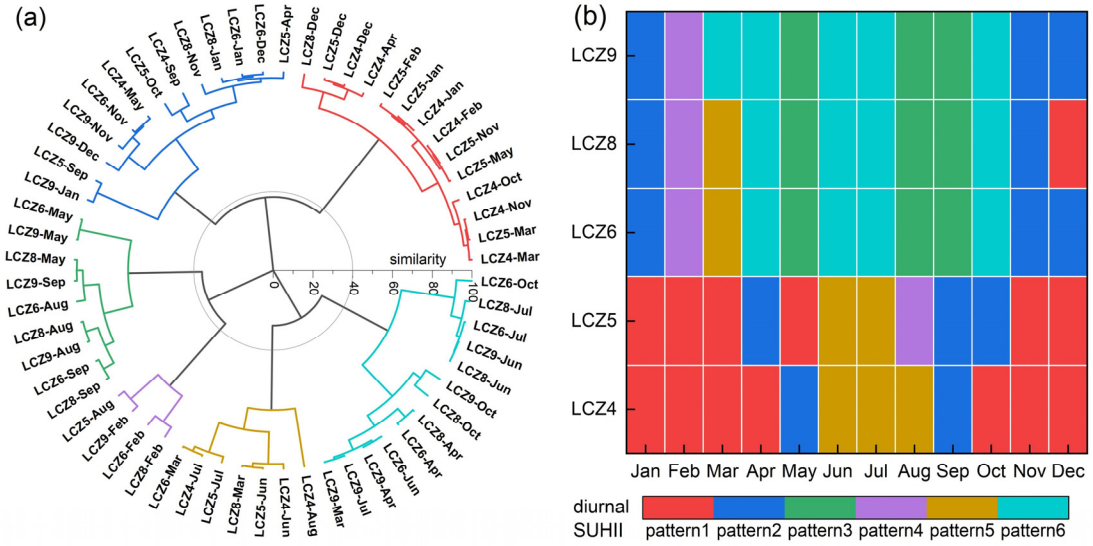

Figure 9. Hierarchical clustering of diurnal SUHII variations across different LCZs and months. (**a**) The spectral plot of clustering patterns, where the 'LCZX-Month' indicates the diurnal variation in LCZ X in that month. (**b**) The division of LCZX-Month into the six major diurnal patterns of SUHIIs.

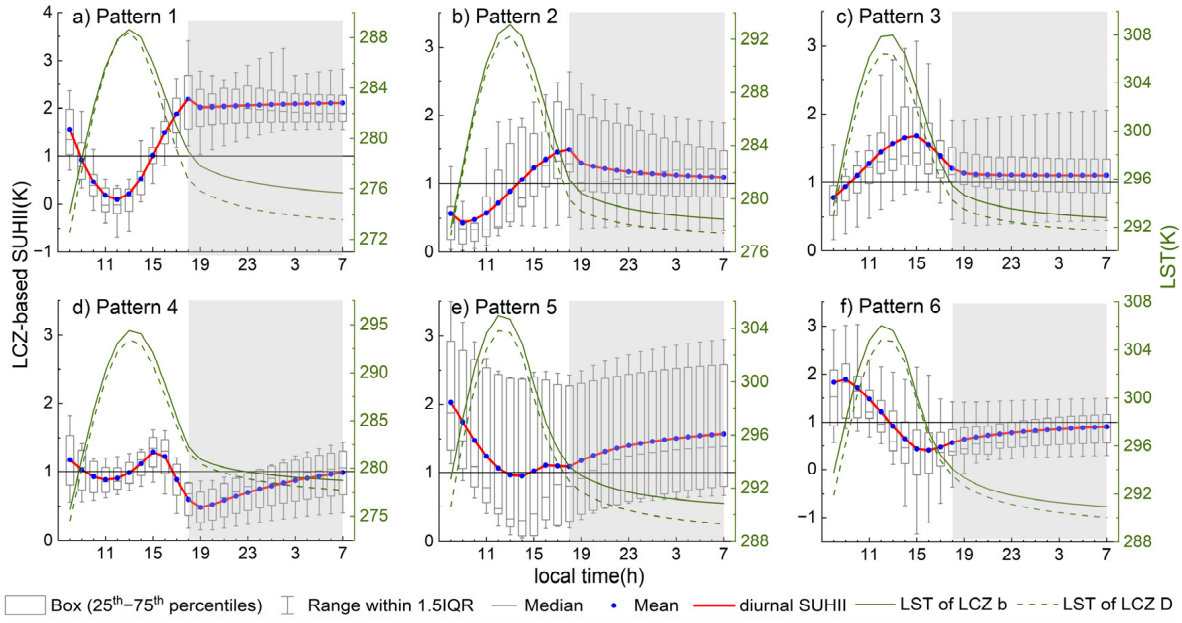

Figure 10. Six major diurnal SUHII patterns of various LCZs and their associated LST cycles in-built LCZ types (LCZ b) and LCZ D. For each pattern, the boxplot includes the contemporaneous SUHIIs in all LCZs and months classified into that pattern in Figure 9, and the mean value is adopted to form the major pattern. Similarly, the associated LSTs are averages among these LCZs and months.

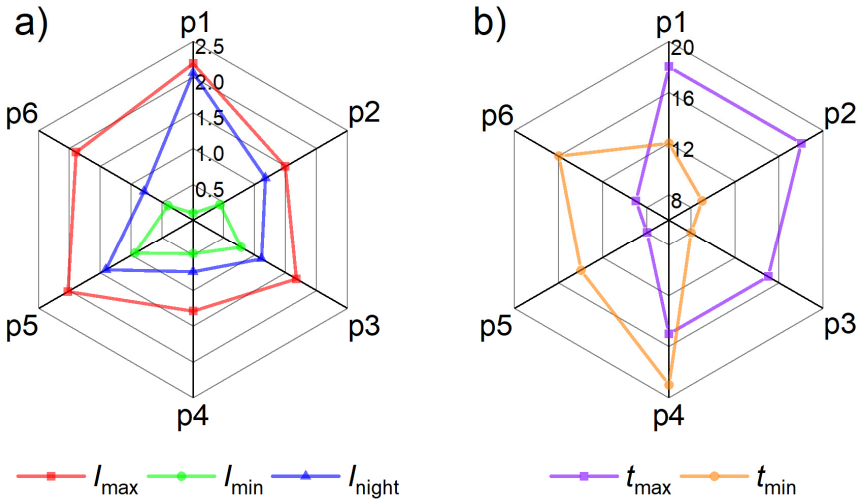

Figure 11. Characteristic parameters of the major diurnal SUHII patterns in Figure 10 (p is an abbreviation for "pattern"). (**a**) shows the maximum SUHII (I_{max}), minimum SUHII (I_{min}) and nocturnal (20:00–04:00) average SUHII (I_{night}), and (**b**) shows the time of I_{max} (t_{max}) and time of I_{min} (t_{min}).

The specific features of the six major diurnal patterns are described as follows.

Pattern one (Figure 10a): SUHII decreases rapidly after sunrise, reaching its lowest value around noon, followed by a sharp increase, exhibiting the highest rate of change during the day among these patterns. After 18:00, SUHII remains consistent at ~2 K, stronger than that during the day. It has the largest I_{max} and I_{night}, and the lowest I_{min} (close to zero), indicating the strongest diurnal variations in SUHII. The LST curves also demonstrate a close resemblance between the built LCZ types and LCZ D around noon, with the most significant differences during the night. This pattern is common in open high- and mid-rise buildings (LCZs 4 and 5), covering most months in winter, spring, and autumn.

Pattern two (Figure 10b): SUHII shows a minor decrease followed by an increase during the day, with a peak around 18:00, and then slightly decreases to around 1.2 K during the night. Its primary difference from pattern one lies in the morning evolution of SUHII and the weaker magnitude of change throughout the day. The short-term decrease in SUHII after sunrise may be attributed to a shadow effect at the low solar altitude that alleviates the heating rate of building types [52]. Nevertheless, the shadow effect will soon be overpowered by the contrasting thermal inertia difference between buildings and low plants as the solar altitude increases with time, leading to a subsequent rise in SUHII. This rationalizes why this pattern occurs mostly in low-rise buildings (LCZs 6, 8, and 9) in winter and high-/mid-rise buildings (LCZs 4 and 5) in April–May and September–October.

Pattern three (Figure 10c): SUHII continues to increase until a prominent peak appears around 15:00, followed by a decrease until ~19:00 and constancy at ~1 K throughout the night. This pattern is present in low-rise buildings (LCZs 6, 8, and 9) in May, August, and September. It differs from all the other patterns in the continuous rise of SUHII from morning to early afternoon, which is probably related to the dominant cooling effect of abundant vegetation coverage in LCZ D in growing seasons.

Pattern four (Figure 10d): SUHII exhibits a peak around 15:00 and two valleys around 11:00 and 19:00, with a gradual increase during the night. The overall SUHII and diurnal variations are weak, mostly ranging from 0.5 K to 1 K. This pattern occurs less frequently than others, appearing only in LCZs 6, 8, and 9 in February and LCZ 5 in August.

Pattern five (Figure 10e): SUHII decreases until ~14:00 and then rises slowly to around 1.5 K for the rest of the day. This pattern maintains a relatively high level of SUHII (>1 K) throughout the day in comparison to others. It primarily occurs in LCZs 4 and 5 during June–August.

Pattern six (Figure 10f): SUHII rises just before 9:00, drops from about 2 K to 0.5 K by ~16:00, and then slowly rises to around 1 K. This pattern is often observed in LCZs 6, 8, and 9 and from April to October.

4.3. Individual and Interactive Effects of Driving Factors

Table 3 shows that the explanatory power of each driving factor exhibits significant seasonal and day–night differences, where all q-values pass the significance test ($p < 0.01$), except for those of MNDWI, BH, and PRS during the spring daytime. In general, the explanatory power is lower in spring than in other seasons, which may be attributed to the significant reduction in human activities during the COVID-19 lockdown in Beijing and the associated substantial weakening of SUHII and spatial variations [53]. For daytime spatial differentiations of SUHIIs, EVI, and GDP have the top two impact degrees in all four seasons, while BSF, PD, RD, and RHU rank third from spring to winter, respectively. TEM has the largest explanatory power for nighttime spatial differentiations of SUHIIs across seasons, which is followed by PD and RD in spring and by EVI and RHU in summer–winter. In terms of mean q-value, the top three factors are EVI > TEM > GDP = RHU, while MNDWI exhibits the least explanatory power.

Table 3. The geodetector q statistic of each driving factor on the spatial stratified heterogeneity of SUHIIs across four seasons and day–night periods.

Factors	Spring		Summer		Autumn		Winter		Average
	Day	Night	Day	Night	Day	Night	Day	Night	
Morphological Factors									
EVI	**0.21**	0.32	**0.60**	**0.66**	**0.58**	**0.63**	**0.23**	**0.54**	**0.47**
MNDWI	0.04 *	0.14	0.19	0.22	0.14	0.23	0.06	0.19	0.15
BSF	**0.19**	0.15	0.26	0.21	0.30	0.18	0.19	0.17	0.21
BH	0.02 *	0.22	0.12	0.37	0.08	0.20	0.03	0.34	0.17
Socioeconomic Factors									
GDP	**0.21**	0.45	**0.37**	0.41	**0.43**	0.46	**0.32**	0.45	**0.39**
PD	0.08	**0.52**	**0.28**	0.46	0.34	0.44	0.22	0.46	0.35
RD	0.08	**0.47**	0.19	0.41	**0.42**	0.52	0.20	0.45	0.34
Meteorological Factors									
PRS	0.02 *	0.27	0.27	0.36	0.16	0.28	0.13	0.26	0.22
RHU	0.15	0.44	**0.28**	**0.57**	0.26	**0.53**	**0.26**	**0.64**	**0.39**
TEM	0.11	**0.61**	0.16	**0.73**	0.15	**0.73**	0.10	**0.71**	**0.41**
Ranking of the 10 factors for each column									10 th → 1 st

* $p > 0.01$.

Among the morphological factors, EVI exhibits the strongest average explanatory power. Particularly during the summer daytime, a q-value of up to 0.60 is obtained. This is mainly due to the well-known cooling effect via vegetation evapotranspiration and canopy shading [54]. Accordingly, the q-value of EVI gradually changes with vegetation phenology and solar insolation, reaching the lowest value during the daytime of cold (leaf-off) seasons [34]. EVI also presents significant controls ($q \geq 0.54$) on the spatial differentiations of summer, autumn, and winter nighttime SUHIIs, which is most likely related to the albedo-induced radiative warming effect of plant canopies [55]. This is consistent with the pronounced nocturnal variation characteristics of LSTs/SUHIIs among LCZs (Figures 7–11). Meanwhile, as many studies have noted, BSF is a key factor influencing the local-scale thermal differentiation [56], especially during the daytime when building canyons and materials demonstrate strong heat storage capacities and eventually substantial contributions to increased SUHIIs [57]. In contrast to BSF, BH exhibits a higher explanatory power for the nighttime SUHIIs ($0.20 \leq q \leq 0.37$) than for the daytime SUHIIs ($0.02 \leq q \leq 0.12$). This supports to some extent the general dichotomy between high-/mid-rise buildings (LCZs 4 and 5) and low-rise buildings (LCZs 6, 8, and 9) in terms of major diurnal SUHII patterns

with significant I_{night} differences in each month (Figures 9 and 11). The overall explanatory power of BH is slightly lower than that of BSF.

Among the socioeconomic factors, GDP has the strongest power to explain the daytime SUHII variations ($0.21 \leq q \leq 0.43$), which could be attributed to its comprehensiveness with respect to PD and RD regarding human activity, surface morphology, and zonal function. For nighttime SUHII variations, GDP, PD, and RD show close contribution magnitudes (0.41–0.52), mainly revealing the impact of anthropogenic heat emissions [58]. Among them, PD and RD are the second- and third-ranked explanatory variables during the spring nighttime. One possible reason for this is the strict COVID-19 lockdown in Beijing in the spring of 2020, which has led to reduced human mobility and increased transportation of goods, thus maybe increasing the explanatory powers of the annual PD and RD datasets at night.

Among the meteorological factors, TEM plays a dominant role in determining the spatial variation in nighttime SUHIIs, with an explanatory power ranging from 61% to 73%. This is consistent with previous studies, indicating a strong correlation between nighttime atmospheric and surface temperatures [59]. Research has also suggested that nighttime humidity can control surface cooling [60], which may explain the higher explanatory power of RHU (44% to 64%) at night. On the other hand, the daytime q-values of TEM and RHU are notably lower. This could be attributed to the fact that the daytime SUHII mechanism is more complex [61] and influenced more by surface morphology and human activities. Compared to RHU and TEM, the influence of PRS on the spatial variation in SUHIIs is limited.

Furthermore, interactive effects among 10 driving factors are shown in Figure 12. The interaction types are either two-factor enhancement or nonlinear enhancement, indicating that the driving effects on SUHII are not independent but rather interdependent, and the interaction between any two factors can enhance the impact on SUHIIs. The nonlinear enhancement interaction primarily occurs during the daytime, while nighttime interactions are mostly categorized as two-factor enhancement, implying that the daytime driving mechanism may be more complex than the nighttime counterpart.

During the spring daytime, all the interactions are nonlinear enhancement. The largest individual effect is 0.21 (q(EVI) and q(GDP)), while the interactive effect can reach 0.53 (q(TEM $\cap$ GDP)) and 0.51 (q(RHU $\cap$ GDP)). This may suggest that the urban thermal environment in the spring of 2020 is more dependent on the response of local socioeconomics to variable meteorological conditions. The winter daytime has the second largest number of factor pairs with nonlinear enhancement. Particularly, MNDWI, BH, PRS, and TEM have extremely low individual effects; nonetheless, their explanatory powers are highly strengthened by nonlinear interactions with any other factor. In summer and autumn, the strongest interaction factors for daytime SUHIIs are EVI $\cap$ GDP, EVI $\cap$ PD, EVI $\cap$ RHU, and EVI $\cap$ TEM ($q \geq 0.69$). They are also the factors with the highest individual effects (Table 3). During the nighttime, the top three interactive effects always involve TEM, regardless of the season. This further confirms the substantial part played by TEM in characterizing the nighttime thermal patterns, whether as a single factor or interacting with other factors.

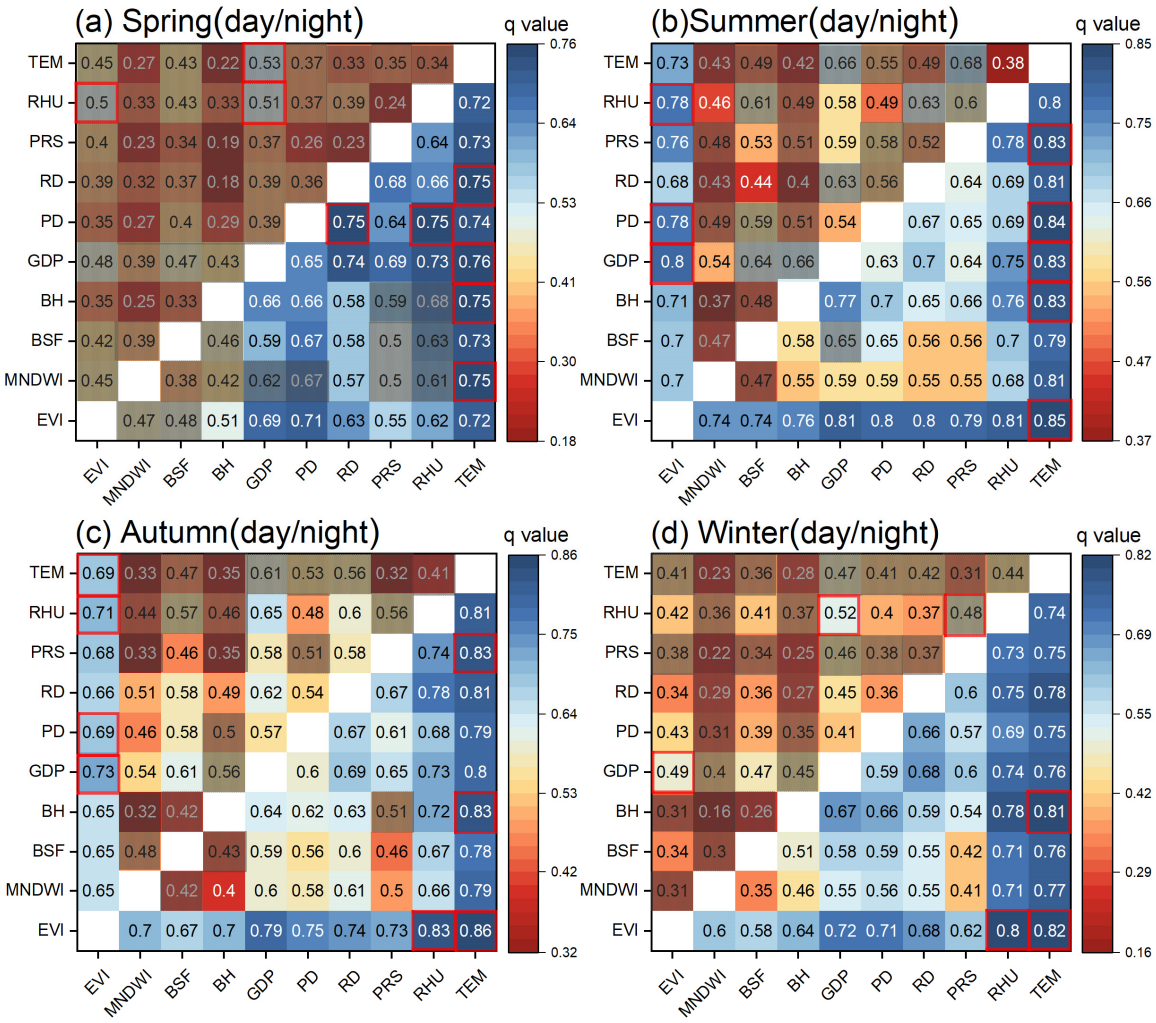

Figure 12. Interactive effects (q(X1 ∩ X2)) among 10 driving factors on the seasonal and day–night spatial differentiations of SUHIIs. The upper and lower triangles show the daytime and nighttime results, respectively. The red frames indicate the top three *q*-values for each scenario. The shadowed squares represent the nonlinear enhancement effect, while the others represent two-factor enhancement.

5. Discussion

This study focused on the combined use of a series of methods (i.e., DTC modeling, LCZ mapping, hierarchical clustering, and geodetector analysis) to identify the major diurnal patterns of SUHIIs of built LCZ types and the driving factors for spatial differentiations of SUHIIs that have not been fully understood before. It mainly innovated in three aspects. First, SUHIIs based on an LCZ scheme were comprehensively examined at a continuous diurnal scale and over 12 months. Second, six major diurnal patterns of SUHIIs were generalized and elucidated in detail across different built LCZ types and months based on hierarchical clustering analysis. Third, the spatial stratified heterogeneity of SUHIIs during four seasons and day–night periods was explored from both individual and interactive perspectives using the geodetector.

The results contribute to expanding our understanding of the diurnal variations in the local thermal environment associated with different types of urban buildings and the complex driving effects of urban morphological, socioeconomic, and meteorological conditions. For example, the major pattern one and pattern two identified in this study accord well with the "weak-spoon" pattern and "quasi-spoon" pattern defined by Lai et al. [52], respectively; nevertheless, the major patterns 3–6 are not recognized as the

typical diurnal patterns of SUHIIs in their study. This is mainly because they focused on nationwide cities with higher levels of urbanization based on the urban–rural dichotomy and thus may have difficulties capturing the diurnal variations primarily associated with low-rise buildings (LCZs 6, 8, and 9). Pattern one was found common in open high- and mid-rise buildings (LCZs 4 and 5) in winter, spring, and autumn. This rationalizes the diurnal SUHII change during this period in Beijing characterized by an urban–rural delineation in the study of Zhou et al. [62], as LCZs 4 and 5 have larger numbers and greater variations than other built LCZ types and exert a higher impact on the urban-averaged SUHII. This pattern also supports Dong et al. [16] on the transition of SUHII around sunset for high-rise built LCZ types in winter. Moreover, unlike many previous studies [63,64], this study obtained a high q-value ($\geq$0.54) of EVI for explaining the spatial SUHII differentiations during the summer, autumn, and winter nighttime. This difference may be due to the fact that the geodetector here measures the zonal heterogeneity affected by drivers, while previous studies primarily evaluate the pixel-by-pixel linear relationship, further indicating that the vegetation albedo-based radiative effect on the nighttime SUHII is likely to be nonlinear and/or hierarchical [52]. Meanwhile, EVI presents the strongest interaction effects with GDP, PD, RHU and TEM during the summer and autumn daytime, implying that it is important to reasonably configure the spatial distribution of vegetation with locally specific socioeconomic and climatological conditions for further surface heat mitigation in warm/hot seasons.

Despite these progresses, this study has certain limitations and future aspects as follows.

(1) In terms of the LST reconstruction and LCZ classification

The DTC model describes clear-sky LST evolutions and requires at least four observations per day; therefore, the diurnal LSTs were reconstructed under the assumption of 24 h of cloudlessness with a resolution of 1 km on a monthly basis. This could lead to slightly reduced magnitudes of spatiotemporal variations in LCZ-based SUHIIs [11], difficulties in characterizing practical diurnal thermal patterns under all-weather/overcast/rainy conditions [65], and the lack of appropriateness in tropical and high-latitude regions [66]. The use of microwave and/or reanalysis data associated with sophisticated spatiotemporal reconstruction models to generate all-weather diurnal high-resolution LSTs [67] would improve the stability and comprehensiveness of the research results. However, such products are not currently accessible, and advanced data modeling is not the focus of the current study. Considering that this study mainly concentrated on the major building LCZ types that have certain aggregation features with sufficient sizes, it is inferred that the overall patterns of diurnal variations are less affected during the clustering analysis and most likely still hold at a higher spatial resolution. Another caveat of the DTC model is that it does not incorporate the directionality of thermal radiation with urban 3D structures and multi-angle satellite observations. This may disturb the diurnal curves of SUHIIs in vertical buildings, reduce their comparability over space and time, and lower the explanatory powers of 3D morphological factors [68]. Additionally, the GIS-based LCZ mapping approach heavily depends on high-resolution 3D building and plant information, which are often unavailable, particularly in under-developed countries and cities. Therefore, it is desirable to adopt/develop a more widely applicable yet highly accurate LCZ classification framework to further explore the diurnal SUHII patterns of different LCZ types across multiple cities or even globally.

(2) In terms of the geographical detection

The geodetector is susceptible to a partitioning effect, meaning that different methods of discretizing and classifying independent variables would affect the attribution results to some extent [69]. Therefore, following previous research [37,69], we classified all independent variables into the same number of classes using the quantile classification method and made analyses based on the relative importance or ranks among driving factors. Further improvements in the reclassification of drivers may consider the regional characteristics

of each independent variable. Also, incorporating a sufficient number of driving factors helps avoid fortuitous outcomes of geographical detection. Here, we combined 10 factors covering distinct perspectives of urban morphology, socioeconomics, and meteorology. However, due to the limited access to frequent records of socioeconomic conditions, yearly data were used for seasonal and day–night attribution analysis. This may introduce biases in assessing the multi-temporal impacts of socioeconomic activities [70], which could be mitigated by utilizing real-time data on crowd statistics and behaviors (e.g., mobile phone and microblogging) as well as anthropogenic heat emissions. In addition, while the geodetector enables analysis of both single-factor and interaction-factor effects, it is still limited in capturing the collective interactions among multiple driving factors, which are crucial for gaining a comprehensive understanding of complex geographic phenomena.

6. Conclusions

In this study, we first reconstructed diurnal LSTs of Beijing in 2020 using MODIS LST data and a DTC model. Combined with the LCZ classification, we then analyzed the multi-temporal thermal characteristics of different LCZs. On this basis, diurnal SUHII patterns were clustered across different built LCZ types and months, and their characteristic parameters were identified. The geodetector q statistic was further employed to investigate the driving mechanisms behind multi-temporal spatial differentiations in SUHIIs in association with the urban morphological, socioeconomic, and meteorological factors. The main conclusions are as follows:

(1) There exist six primary diurnal SUHII patterns among five main built types and 12 months. LCZs 4 and 5 (open high- and mid-rise) predominantly exhibit patterns one, two, and five, with an increase in SUHII in the afternoon, which is maintained at higher values (I_{night} > 1.2 K) at night. LCZs 6, 8, and 9 (open, large, and sparsely-built low-rise) mainly display patterns three, four, and six, with a decrease in SUHII during the afternoon and lower intensities at night ($I_{night} \leq$ 1.2 K). $t_{\max}$ and $t_{\min}$ for patterns 1–3 are in the afternoon–evening, and morning, respectively, whereas those for patterns 5–6 are in the morning and afternoon, respectively.

(2) EVI and GDP have the top two explanatory powers for daytime spatial differentiations of SUHIIs in all four seasons, while BSF, PD, RD, and RHU rank third from spring to winter. TEM has the strongest individual effect for nighttime spatial differentiations of SUHIIs, followed by PD and RD in spring and EVI and RHU in summer–winter.

(3) Factor interaction types are two-factor and nonlinear enhancement across four seasons. The former/latter mainly exists during the nighttime/daytime, where the nighttime explanatory powers are greater than the daytime ones. The strongest interactions are EVI ∩ GDP (q = 0.80) during the day and TEM ∩ EVI (q = 0.86) at night.

Future works may incorporate sophisticated models for diurnal all-weather LST reconstruction with a high spatial resolution covering 3D facets, examine diurnal LCZ-based SUHIIs for varied cities and climates by combining widely applicable yet highly accurate LCZ classification frameworks, and explore collective interactions among dynamic driving factors for a further comprehensive understanding of the complex SUHI phenomena.

Author Contributions: Conceptualization, J.Q. and T.M.; Methodology, Y.G. and J.Q.; Investigation and Data Curation, Y.G.; Writing—Original Draft, Y.G. and J.Q.; Writing—Review and Editing, J.Q., T.M., S.C., C.X. and J.G. All authors have read and agreed to the published version of the manuscript.

Funding: The Youth Project of Innovation LREIS (YPI008); the Youth Innovation Promotion Association, CAS (2021051).

Conflicts of Interest: The authors declare no conflict of interest.

References

1. Oke, T.R. The energetic basis of the urban heat island. *Q. J. R. Meteorol. Soc.* **1982**, *108*, 1–24. [CrossRef]
2. Rizwan, A.M.; Dennis, L.Y.C.; Liu, C. A review on the generation, determination and mitigation of Urban Heat Island. *J. Environ. Sci.* **2008**, *20*, 120–128. [CrossRef] [PubMed]
3. Voogt, J.A.; Oke, T.R. Thermal remote sensing of urban climates. *Remote Sens. Environ.* **2003**, *86*, 370–384. [CrossRef]
4. Zhou, D.; Zhao, S.; Liu, S.; Zhang, L.; Zhu, C. Surface urban heat island in China's 32 major cities: Spatial patterns and drivers. *Remote Sens. Environ.* **2014**, *152*, 51–61. [CrossRef]
5. Kong, J.; Zhao, Y.; Carmeliet, J.; Lei, C. Urban heat island and its interaction with heatwaves: A review of studies on mesoscale. *Sustainability* **2021**, *13*, 10923. [CrossRef]
6. Mishra, V.; Ganguly, A.R.; Nijssen, B.; Lettenmaier, D.P. Changes in observed climate extremes in global urban areas. *Environ. Res. Lett.* **2015**, *10*, 024005. [CrossRef]
7. Chu, P.; Jiang, Z.; Li, Q.; Dong, L. Analysis of the effect of uncertainty in urban and rural classification on urbanization impact assessment. *Trans. Atmos. Sci.* **2016**, *39*, 661–671. [CrossRef]
8. Bechtel, B.; Demuzere, M.; Mills, G.; Zhan, W.; Sismanidis, P.; Small, C.; Voogt, J. SUHI analysis using local climate zones—A comparison of 50 cities. *Urban Clim.* **2019**, *28*, 100451. [CrossRef]
9. Verdonck, M.-L.; Okujeni, A.; van der Linden, S.; Demuzere, M.; De Wulf, R.; Van Coillie, F. Influence of neighbourhood information on 'Local Climate Zone' mapping in heterogeneous cities. *Int. J. Appl. Earth Obs. Geoinf.* **2017**, *62*, 102–113. [CrossRef]
10. Oke, T.R.; Stewart, I.D. Local climate zones for urban temperature studies. *Bull. Am. Meteorol. Soc.* **2012**, *93*, 1879–1900. [CrossRef]
11. Jiang, S.; Zhan, W.; Yang, J. Urban heat island studies based on local climate zones: A systematic overview. *Acta Geogr. Sin.* **2020**, *75*, 1860–1878. [CrossRef]
12. Kaloustian, N.; Bechtel, B. Local climatic zoning and urban heat island in Beirut. *Procedia Eng.* **2016**, *169*, 216–223. [CrossRef]
13. Beck, C.; Straub, A.; Breitner, S.; Cyrys, J.; Philipp, A.; Rathmann, J.; Schneider, A.; Wolf, K.; Jacobeit, J. Air temperature characteristics of local climate zones in the Augsburg urban area (Bavaria, southern Germany) under varying synoptic conditions. *Urban Clim.* **2018**, *25*, 152–166. [CrossRef]
14. Leconte, F.; Bouyer, J.; Claverie, R.; Pétrissans, M. Using local climate zone scheme for UHI assessment: Evaluation of the method using mobile measurements. *Build. Environ.* **2015**, *83*, 39–49. [CrossRef]
15. Stewart, I.D.; Oke, T.R.; Krayenhoff, E.S. Evaluation of the 'Local Climate Zone' scheme using temperature observations and model simulations. *Int. J. Climatol.* **2014**, *34*, 1062–1080. [CrossRef]
16. Dong, P.; Jiang, S.; Zhan, W.; Wang, C.; Miao, S.; Du, H.; Li, J.; Wang, S.; Jiang, L. Diurnally continuous dynamics of surface urban heat island intensities of local climate zones with spatiotemporally enhanced satellite-derived land surface temperatures. *Build. Environ.* **2022**, *218*, 109105. [CrossRef]
17. Xia, H.; Chen, Y.; Song, C.; Li, J.; Quan, J.; Zhou, G. Analysis of surface urban heat islands based on local climate zones via spatiotemporally enhanced land surface temperature. *Remote Sens. Environ.* **2022**, *273*, 112972. [CrossRef]
18. Yang, X.; Yao, L.; Jin, T.; Peng, L.L.H.; Jiang, Z.; Hu, Z.; Ye, Y. Assessing the thermal behavior of different local climate zones in the Nanjing metropolis, China. *Build. Environ.* **2018**, *137*, 171–184. [CrossRef]
19. Geletič, J.; Lehnert, M.; Savić, S.; Milošević, D. Inter-/intra-zonal seasonal variability of the surface urban heat island based on local climate zones in three central European cities. *Build. Environ.* **2019**, *156*, 21–32. [CrossRef]
20. Quan, J. Multi-temporal effects of urban forms and functions on urban heat islands based on local climate zone classification. *Int. J. Env. Res. Public Health* **2019**, *16*, 2140. [CrossRef]
21. Stewart, I.D.; Krayenhoff, E.S.; Voogt, J.A.; Lachapelle, J.A.; Allen, M.A.; Broadbent, A.M. Time evolution of the surface urban heat island. *Earth's Future* **2021**, *9*, 2178. [CrossRef]
22. Hu, J.; Yang, Y.; Pan, X.; Zhu, Q.; Zhan, W.; Wang, Y.; Ma, W.; Su, W. Analysis of the spatial and temporal variations of land surface temperature based on local climate zones: A case study in Nanjing, China. *IEEE J. Sel. Top. Appl. Earth Obs. Remote Sens.* **2019**, *12*, 4213–4223. [CrossRef]
23. Anniballe, R.; Bonafoni, S.; Pichierri, M. Spatial and temporal trends of the surface and air heat island over Milan using MODIS data. *Remote Sens. Environ.* **2014**, *150*, 163–171. [CrossRef]
24. Roth, M.; Oke, T.R.; Emery, W.J. Satellite-derived urban heat islands from three coastal cities and the utilization of such data in urban climatology. *Int. J. Remote Sens.* **2007**, *10*, 1699–1720. [CrossRef]
25. Chang, Y.; Xiao, J.; Li, X.; Middel, A.; Zhang, Y.; Gu, Z.; Wu, Y.; He, S. Exploring diurnal thermal variations in urban local climate zones with ECOSTRESS land surface temperature data. *Remote Sens. Environ.* **2021**, *263*, 112544. [CrossRef]
26. Jiang, Y.; Fu, P.; Weng, Q. Assessing the impacts of urbanization-associated land use/cover change on land surface temperature and surface moisture: A case study in the midwestern United States. *Remote Sens.* **2015**, *7*, 4880–4898. [CrossRef]
27. Peng, J.; Jia, J.; Liu, Y.; Li, H.; Wu, J. Seasonal contrast of the dominant factors for spatial distribution of land surface temperature in urban areas. *Remote Sens. Environ.* **2018**, *215*, 255–267. [CrossRef]
28. Ramamurthy, P.; Bou-Zeid, E. Heatwaves and urban heat islands: A comparative analysis of multiple cities. *J. Geophys. Res. Atmos.* **2017**, *122*, 168–178. [CrossRef]
29. Arnfield, A.J. Two decades of urban climate research: A review of turbulence, exchanges of energy and water, and the urban heat island. *Int. J. Climatol.* **2003**, *23*, 1–26. [CrossRef]
30. Wang, J.-F.; Hu, Y. Environmental health risk detection with GeogDetector. *Environ. Model. Softw.* **2012**, *33*, 114–115. [CrossRef]

31. You, M.; Lai, R.; Lin, J.; Zhu, Z. Quantitative analysis of a spatial distribution and driving factors of the urban heat island effect: A case study of Fuzhou central area, China. *Int. J. Env. Res. Public Health* **2021**, *18*, 13088. [CrossRef] [PubMed]
32. Zhengming, W.; Dozier, J. A generalized split-window algorithm for retrieving land-surface temperature from space. *IEEE Trans. Geosci. Remote Sens.* **1996**, *34*, 892–905. [CrossRef]
33. Wan, Z. New refinements and validation of the collection-6 MODIS land-surface temperature/emissivity product. *Remote Sens. Environ.* **2014**, *140*, 36–45. [CrossRef]
34. Hu, D.; Meng, Q.; Schlink, U.; Hertel, D.; Liu, W.; Zhao, M.; Guo, F. How do urban morphological blocks shape spatial patterns of land surface temperature over different seasons? A multifactorial driving analysis of Beijing, China. *Int. J. Appl. Earth Obs. Geoinf.* **2022**, *106*, 102648. [CrossRef]
35. Lai, J.; Zhan, W.; Quan, J.; Liu, Z.; Li, L.; Huang, F.; Hong, F.; Liao, W. Reconciling debates on the controls on surface urban heat island intensity: Effects of scale and sampling. *Geophys. Res. Lett.* **2021**, *48*, e2021GL094485. [CrossRef]
36. Hu, Y.; Dai, Z.; Guldmann, J.M. Modeling the impact of 2D/3D urban indicators on the urban heat island over different seasons: A boosted regression tree approach. *J. Env. Manag.* **2020**, *266*, 110424. [CrossRef]
37. Chen, L.; Wang, X.; Cai, X.; Yang, C.; Lu, X. Seasonal variations of daytime land surface temperature and their underlying drivers over Wuhan, China. *Remote Sens.* **2021**, *13*, 323. [CrossRef]
38. Quan, J. Enhanced geographic information system-based mapping of local climate zones in Beijing, China. *Sci. China Technol. Sci.* **2019**, *62*, 2243–2260. [CrossRef]
39. Göttsche, F.-M.; Olesen, F.S. Modelling of diurnal cycles of brightness temperature extracted from METEOSAT data. *Remote Sens. Environ.* **2001**, *76*, 337–348. [CrossRef]
40. Göttsche, F.-M.; Olesen, F.-S. Modelling the effect of optical thickness on diurnal cycles of land surface temperature. *Remote Sens. Environ.* **2009**, *113*, 2306–2316. [CrossRef]
41. Jiang, G.-M.; Li, Z.-L.; Nerry, F. Land surface emissivity retrieval from combined mid-infrared and thermal infrared data of MSG-SEVIRI. *Remote Sens. Environ.* **2006**, *105*, 326–340. [CrossRef]
42. Bergh, F.v.d.; Wyk, M.A.v.; Wyk, B.J.v.; Udahemuka, G. A comparison of data-driven and model-driven approaches to brightness temperature diurnal cycle interpolation. *SAIEE Afr. Res. J.* **2007**, *98*, 81–86. [CrossRef]
43. Inamdar, A.K.; French, A.; Hook, S.; Vaughan, G.; Luckett, W. Land surface temperature retrieval at high spatial and temporal resolutions over the southwestern United States. *J. Geophys. Res. Atmos.* **2008**, *113*, D07107. [CrossRef]
44. Schädlich, S.; Göttsche, F.M.; Olesen, F.S. Influence of land surface parameters and atmosphere on METEOSAT brightness temperatures and generation of land surface temperature maps by temporally and spatially interpolating atmospheric correction. *Remote Sens. Environ.* **2001**, *75*, 39–46. [CrossRef]
45. Duan, S.-B.; Li, Z.-L.; Wang, N.; Wu, H.; Tang, B.-H. Evaluation of six land-surface diurnal temperature cycle models using clear-sky in situ and satellite data. *Remote Sens. Environ.* **2012**, *124*, 15–25. [CrossRef]
46. Meng, X.; Liu, H.; Cheng, J. Evaluation and characteristic research in diurnal surface temperature cycle in China using FY-2F data. *J. Remote Sens.* **2019**, *23*, 570–581. [CrossRef]
47. Wang, J.; Xu, C. Geodetector: Principle and prospective. *Acta Geogr. Sin.* **2017**, *72*, 116–134. [CrossRef]
48. Wang, J.F.; Li, X.H.; Christakos, G.; Liao, Y.L.; Zhang, T.; Gu, X.; Zheng, X.Y. Geographical detectors-based health risk assessment and its application in the neural tube defects study of the Heshun region, China. *Int. J. Geogr. Inf. Sci.* **2010**, *24*, 107–127. [CrossRef]
49. Cheng, J.; Dong, S.; Shi, J. 0.02° Seamless Hourly Land Surface Temperature Dataset over East Asia (2016–2021). 2022. Available online: https://data.tpdc.ac.cn/en/data/06414391-abd4-4d28-a844-bd036a0b8c55/ (accessed on 30 September 2023).
50. Chun, B.; Guhathakurta, S. The impacts of three-dimensional surface characteristics on urban heat islands over the diurnal cycle. *Prof. Geogr.* **2017**, *69*, 191–202. [CrossRef]
51. Erell, E. The application of urban climate research in the design of cities. *Adv. Build. Energy Res.* **2008**, *2*, 95–121. [CrossRef]
52. Lai, J.; Zhan, W.; Huang, F.; Voogt, J.; Bechtel, B.; Allen, M.; Peng, S.; Hong, F.; Liu, Y.; Du, P. Identification of typical diurnal patterns for clear-sky climatology of surface urban heat islands. *Remote Sens. Environ.* **2018**, *217*, 203–220. [CrossRef]
53. Liu, Z.; Lai, J.; Zhan, W.; Bechtel, B.; Voogt, J.; Quan, J.; Hu, L.; Fu, P.; Huang, F.; Li, L.; et al. Urban heat islands significantly reduced by COVID-19 lockdown. *Geophys. Res. Lett.* **2022**, *49*, e2021GL096842. [CrossRef]
54. Berry, R.; Livesley, S.J.; Aye, L. Tree canopy shade impacts on solar irradiance received by building walls and their surface temperature. *Build. Environ.* **2013**, *69*, 91–100. [CrossRef]
55. Alkama, R.; Forzieri, G.; Duveiller, G.; Grassi, G.; Liang, S.; Cescatti, A. Vegetation-based climate mitigation in a warmer and greener World. *Nat. Commun.* **2022**, *13*, 606. [CrossRef] [PubMed]
56. Guo, G.; Zhou, X.; Wu, Z.; Xiao, R.; Chen, Y. Characterizing the impact of urban morphology heterogeneity on land surface temperature in Guangzhou, China. *Environ. Model. Softw.* **2016**, *84*, 427–439. [CrossRef]
57. Liu, W.Y.; Gong, A.D.; Zhou, J.; Zhan, W.F. Investigation on relationships between urban building materials and land surface temperature through a mult-resource remote sensing approach. *Remote Sens. Inf.* **2011**, *31*, 46–53+110. [CrossRef]
58. Wu, X.; Wang, G.; Yao, R.; Wang, L.; Yu, D.; Gui, X. Investigating surface urban heat islands in south America based on MODIS data from 2003–2016. *Remote Sens.* **2019**, *11*, 1212. [CrossRef]
59. Yang, P.; Chen, J.; Hou, X.; Gao, Q.; Zhao, Q. Study of urban heat island based on multi-source data—By the example of the Shijiazhuang area. *Meteorol. Mon.* **2013**, *39*, 1304–1313. [CrossRef]
60. Rongbo, X. A review of the eco-environmental consequences of urban heat islands. *Acta Ecol. Sin.* **2005**, *25*, 2055–2060.

61. Hu, N.; Ren, Z.; Dong, Y.; Fu, Y.; Guo, Y.; Mao, Z.; Chang, X. Spatio-temporal evolution of heat island effect and its driving factors in urban agglomerations of China. *Sci. Geogr. Sin.* **2022**, *42*, 1534–1545. [CrossRef]
62. Zhou, J.; Chen, Y.; Zhang, X.; Zhan, W. Modelling the diurnal variations of urban heat islands with multi-source satellite data. *Int. J. Remote Sens.* **2013**, *34*, 7568–7588. [CrossRef]
63. Lu, Y.; Wu, P.; Ma, X.; Yang, H.; Wu, Y. Monitoring seasonal and diurnal surface urban heat islands variations using Landsat-scale data in Hefei, China, 2000–2017. *IEEE J. Sel. Top. Appl. Earth Obs. Remote Sens.* **2020**, *13*, 6410–6423. [CrossRef]
64. Long, L.; Yong, Z.; Jiahua, Z. Spatial and dynamic perspectives on surface urban heat island and their relationships with vegetation activity in Beijing, China, based on Moderate Resolution Imaging Spectroradiometer data. *Int. J. Remote Sens.* **2020**, *41*, 882–896. [CrossRef]
65. Wang, X.; Zhang, C.; Dong, N.; Yao, W. Urban heat island effect under different meteorological conditions in Jining of Shandong province. *J. Nanjing Univ. Inf. Sci. Technol.* **2016**, *8*, 160–165. [CrossRef]
66. Hong, F.; Zhan, W.; Göttsche, F.M.; Liu, Z.; Dong, P.; Fu, H.; Fan, H.; Zhang, X. A global dataset of spatiotemporally seamless daily mean land surface temperatures: Generation, validation, and analysis. *Earth Syst. Sci. Data* **2022**, *14*, 3091–3113. [CrossRef]
67. Ma, J.; Shen, H.; Wu, P.; Wu, J.; Gao, M.; Meng, C. Generating gapless land surface temperature with a high spatio-temporal resolution by fusing multi-source satellite-observed and model-simulated data. *Remote Sens. Environ.* **2022**, *278*, 113083. [CrossRef]
68. Berger, C.; Rosentreter, J.; Voltersen, M.; Baumgart, C.; Schmullius, C.; Hese, S. Spatio-temporal analysis of the relationship between 2D/3D urban site characteristics and land surface temperature. *Remote Sens. Environ.* **2017**, *193*, 225–243. [CrossRef]
69. Wang, R.; Wang, M.; Zhang, Z.; Hu, T.; Xing, J.; He, Z.; Liu, X. Geographical detection of urban thermal environment based on the local climate zones: A case study in Wuhan, China. *Remote Sens.* **2022**, *14*, 1067. [CrossRef]
70. Sun, Z.J.; Xie, S.Y. Spatiotemporal variation in net primary productivity and factor detection in Yunnan Province based on geodetector. *Chin. J. Ecol.* **2021**, *40*, 3836–3848. [CrossRef]